Quantum Metamaterial for Broadband Detection of Single Microwave Photons

Quantum Metamaterial for Broadband Detection of Single Microwave Photons

Arne L. Grimsmo,[1,2,*] Baptiste Royer,[1,3] John Mark Kreikebaum,[4,5] Yufeng Ye,[6,7] Kevin O'Brien,[6,7] Irfan Siddiqi,[4,5,8] and Alexandre Blais[1,9]

[1] *Institut quantique and Département de Physique, Université de Sherbrooke, Sherbrooke, Québec J1K 2R1, Canada*
[2] *Centre for Engineered Quantum Systems, School of Physics, The University of Sydney, Sydney, Australia*
[3] *Department of Physics, Yale University, New Haven, Connecticut 06520, USA*
[4] *Materials Science Division, Lawrence Berkeley National Laboratory, Berkeley, California 94720, USA*
[5] *Quantum Nanoelectronics Laboratory, Department of Physics, University of California, Berkeley, California 94720, USA*
[6] *Research Laboratory of Electronics, Massachusetts Institute of Technology, Cambridge, Massachusetts 02139, USA*
[7] *Department of Electrical Engineering and Computer Science, Massachusetts Institute of Technology, Cambridge, Massachusetts 02139, USA*
[8] *Computational Research Division, Lawrence Berkeley National Laboratory, Berkeley, California 94720, USA*
[9] *Canadian Institute for Advanced Research, Toronto, Canada*

(Received 14 July 2020; revised 27 January 2021; accepted 1 February 2021; published 25 March 2021)

Detecting traveling photons is an essential primitive for many quantum-information processing tasks. We introduce a single-photon detector design operating in the microwave domain, based on a weakly nonlinear metamaterial where the nonlinearity is provided by a large number of Josephson junctions. The combination of weak nonlinearity and large spatial extent circumvents well-known obstacles limiting approaches based on a localized Kerr medium. Using numerical many-body simulations we show that the single-photon detection fidelity increases with the length of the metamaterial to approach one at experimentally realistic lengths. A remarkable feature of the detector is that the metamaterial approach allows for a large detection bandwidth. The detector is nondestructive and the photon population wavepacket is minimally disturbed by the detection. This detector design offers promising possibilities for quantum information processing, quantum optics and metrology in the microwave frequency domain.

DOI: 10.1103/PhysRevApplied.15.034074

I. INTRODUCTION

In contrast to infrared, optical, and ultraviolet frequencies where single-photon detectors are a cornerstone of experimental quantum optics, the realization of a detector with similar performance at microwave frequencies is far more challenging [1–13]. Due to the small energies of microwave photons, subtle quantum effects such as measurement backaction play a prominent role. A first challenge for single-photon detection is linked to the quantum Zeno effect: continuously and strongly monitoring an absorber will prevent the incoming photon from being absorbed [1,12]. A second difficulty concerns the trade-off between detector efficiency and bandwidth. A large detector response to a single photon requires a sufficiently long interaction time with the photon. As the absorber linewidth is typically inversely proportional to the photon interaction time, this imposes a serious constraint on the detector bandwidth.

The interest in realizing a single-photon detector in the microwave domain is intimately linked to the emergence of engineered quantum systems whose natural domain of operations is in the microwaves, including superconducting quantum circuits [14,15], semiconductor quantum dots [16], spin ensembles [17], and mechanical quantum oscillators [18]. The continuing improvement in coherence and control over these quantum systems offers a wide range of applications for microwave single-photon detection, such as photon-based quantum computing [19], modular quantum-computing architectures [20], high-precision sensing [21], and the detection of dark-matter axions [22].

A number of theoretical proposals and experimental demonstrations of microwave single-photon detectors have emerged recently. These schemes can broadly be divided into two categories: time-gated schemes where accurate information about the photon's arrival time is needed *a priori* [2,6,7,10,11,13], and detectors that operate continuously in time and attempt to accurately record the photon arrival time [1,3–5,8,9,12,13]. In this work, we are concerned with the latter category, which is simultaneously

*arne.grimsmo@sydney.edu.au

the most challenging to realize and finds the widest range of applications.

Depending on the intended application, there are several metrics characterizing the usefulness of single-photon detectors. Not only is high single-photon detection fidelity required for many quantum-information applications, but large bandwidth, fast detection, and short dead times are also desirable [23]. Moreover, nondestructive photon counting is of fundamental interest and offers possibilities for quantum measurement and control not achievable with destructive detectors. In this paper, we introduce the Josephson traveling-wave photodetector (JTWPD), a nondestructive single-photon detector, which we predict to have remarkably high performance across the mentioned metrics. We numerically estimate detection fidelities approaching unity for realistic parameters, without sacrificing detector bandwidth or requiring long detection or reset times.

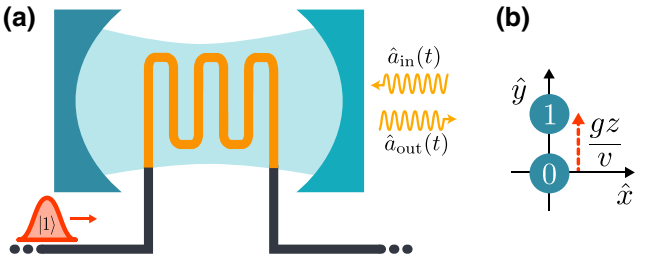

FIG. 1. (a) Sketch of the JTWPD. Standard transmission lines (black) are coupled to both ends of a one-dimensional metamaterial (orange) of length z and linear dispersion relation, $\omega = vk$. A cross-Kerr interaction χ between the metamaterial and the giant probe mode (blue) leads to a phase shift in the strong measurement tone (yellow) while the signal photon (red) travels through the metamaterial. (b) Phase-space picture of the probe mode. With respect to the idle coherent state $|\alpha\rangle$, the presence of a signal photon displaces the states by gz/v, with $g = \chi\alpha$.

II. JTWPD DESIGN AND WORKING PRINCIPLE

The JTWPD exploits a weakly nonlinear, one-dimensional metamaterial, designed to respond to the presence of a single photon. The nonlinearity is provided by a large number of Josephson junctions, inspired by the Josephson traveling-wave parametric amplifier [24]. Because the detector response does not rely on any resonant interaction, the detector bandwidth can be designed to range from tens of MHz to the GHz range. The SNR grows linearly with the length of the metamaterial, which can be made large, leading to single-photon detection fidelities approaching unity. By interrogating the nonlinear medium with a "giant probe" [25]—a probe system that couples to the medium over a spatial extent that is non-negligible compared to the length of the signal photons—this approach bypasses previous no-go results for photon counting based on localized cross-Kerr interactions [26–29].

The JTWPD is illustrated schematically in Fig. 1: in place of a localized absorber as used in previous proposals [1,3–5,12,13], we use a long and weakly nonlinear metamaterial. Backscattering is avoided by using a nonlinearity that is locally weak, yet a large response is made possible by having a long photon time of flight through the metamaterial. Since the photon is never localized, the backaction on the photon wave vector is minimized. This approach allows us to overcome the limitations on detector fidelity and bandwidth present in previous schemes.

The presence of a photon is recorded using a continuously monitored probe mode that is coupled to the metamaterial along the full extent of its length. Thanks to a nonlinear cross-Kerr coupling, in the presence of the measurement tone $\hat{a}_{\rm in}(t)$, a single photon in the metamaterial induces a displacement of the output field $\hat{a}_{\rm out}(t)$ relative to its idle state. While the interaction between the metamaterial and the probe mode is locally too weak to cause any noticeable change in $\hat{a}_{\rm out}(t)$, the displacement accumulates as the photon travels through the metamaterial leading to a large enough signal to be recorded using homodyne detection.

As illustrated in Fig. 2, the backbone of the metamaterial is a waveguide of length z (orange) realized as a linear chain of coupled LC oscillators, in a configuration known as composite right- and left-handed (CRLH) metamaterial [30]. The LC oscillators are coupled via an array of nonlinear couplers to a readout resonator acting as a giant probe (blue). The couplers (inset) are based on a superconducting loop with a single small junction and a number of larger junctions, operated at a point where the nonlinear potential of the couplers is given by $\hat{U}_Q(\hat{\varphi}) = E_Q\hat{\varphi}^4/24 + \ldots$, with $\hat{\varphi}$ the superconducting phase difference across the coupler, $E_Q > 0$ quantifies the nonlinearity, and the ellipses refer to higher-order terms. See Appendix A for further details. This circuit has been dubbed the "quarton" due to the purely nonlinear quartic potential [31].

With the metamaterial coupled at $x = \pm z/2$ to impedance-matched linear transmission lines, the interaction time between the photon and the giant probe is $\tau = z/v$, where v is the speed of light in the metamaterial. As an alternative to this transmission mode, the interaction time can be doubled by terminating the metamaterial at $x = +z/2$ with an open where the photon wavepacket is reflected. To simplify the analysis, we consider the transmission mode in most of the treatment below, but return to a discussion of reflection mode when discussing potential experimental implementation and parameters.

The full detector Hamiltonian can be expressed as $\hat{H} = \hat{H}_0 + \hat{H}_r + \hat{H}_{\rm int}$, where $\hat{H}_0$ contains the linear part of the waveguide including the metamaterial as well as the input and output linear waveguides, $\hat{H}_r$ is the probe resonator Hamiltonian and $\hat{H}_{\rm int}$ describes the nonlinear coupling

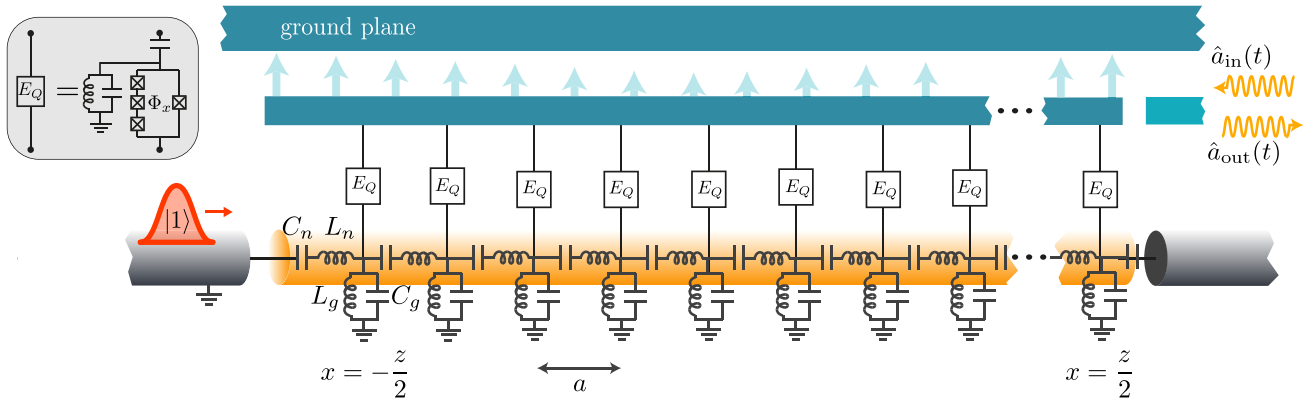

FIG. 2. Schematic representation of the JTWPD. The probe resonator with ground plane on top and the center conductor below (blue), as well as a readout port on the right, acts as a giant probe. The light blue arrows illustrate the fundamental mode function of a $\lambda/2$ resonator. The probe resonator is coupled via a position-dependent cross-Kerr interaction $\chi(x)$, mediated by an array nonlinear quarton couplers (inset), to a metamaterial waveguide (orange). The metamaterial is coupled to impedance matched input and output transmission lines at $x = -z/2$ and $x = z/2$ (gray). An incoming photon of Gaussian shape $\xi(x,t)$ is illustrated (red).

between the probe and the metamaterial. As shown within the Supplemental Material [32], in the continuum limit where the size a of a unit cell of the metamaterial is small with respect to the extent of the photon wavepacket, $\hat{H}_0$ takes the form

$$\hat{H}_0 = \sum_{\nu=\pm} \int_\Omega d\omega \hbar\omega \hat{b}^\dagger_{\nu\omega} \hat{b}_{\nu\omega}. \tag{1}$$

In this expression, $\hat{b}^\dagger_{\pm\omega}$ creates a delocalized right- or left-moving photon with energy $\hbar\omega$ and satisfies the canonical commutation relation $[\hat{b}_{\nu\omega}, \hat{b}^\dagger_{\mu\omega'}] = \delta_{\nu\mu}\delta(\omega-\omega')$. The subscript Ω in Eq. (1) is used to indicate that we consider only a band of frequencies around which the metamaterial's dispersion relation is approximately linear. The probe resonator Hamiltonian $\hat{H}_r$ can be written in a displaced and rotating frame with respect to the coherent drive field as (see Appendix B)

$$\hat{H}'_r = \frac{\hbar K}{2} \hat{a}^{\dagger 2} \hat{a}^2, \tag{2}$$

where we for simplicity include only a single resonator mode, described by a creation (annihilation) operator $\hat{a}^\dagger$ ($\hat{a}$), and K is a self-Kerr nonlinearity induced by the nonlinear couplers.

The nonlinear coupling elements also lead to cross-Kerr interaction between the array of oscillators and the probe mode. As mentioned above, this coupling is chosen to be locally weak such that the nonlinearity is only activated by the presence of a strong coherent drive $\hat{a}_{\rm in}(t)$ on the probe. In this limit, the nonlinear interaction Hamiltonian $\hat{H}_{\rm int}$ is in the same rotating and displaced frame given by (see Appendix C)

$$\hat{H}'_{\rm int} = \hbar \sum_{\nu\mu} \int_{-z/2}^{z/2} dx \chi(x) \hat{b}^\dagger_\nu(x) \hat{b}_\mu(x) \left(\hat{a}^\dagger \hat{a} + \alpha^2\right) + \hbar \sum_{\nu\mu} \int_{-z/2}^{z/2} dx g(x) \hat{b}^\dagger_\nu(x) \hat{b}_\mu(x) \left(\hat{a}^\dagger + \hat{a}\right), \tag{3}$$

where we define the x-dependent photon annihilation operators

$$\hat{b}_\nu(x) = \sqrt{\frac{\bar{\omega}}{2\pi v}} \int_\Omega \frac{d\omega}{\sqrt{\omega}} \hat{b}_{\nu\omega} e^{\nu i\omega x/v}, \tag{4}$$

with $\bar{\omega}$ a nominal center frequency for the incoming photon, which is introduced here for later convenience. The parameter $\chi(x)$ is a dispersive shift per unit length given in Eq. (C2), while $g(x) = \alpha\chi(x)$ with α the displacement of the probe resonator field under the strong drive $\hat{a}_{\rm in}$. The expression for α, which we take to be real without loss of generality, is given in Eq. (B6).

As can be seen from the second term of Eq. (3), which dominates for small $\chi(x)$ and large α, the combined effect of the cross-Kerr coupling and the strong drive results in a longitudinal-like interaction between the metamaterial and the probe mode [33]. This corresponds to a photon-number-dependent displacement of the probe field relative to the idle-state displacement α, which accumulates when a photon travels along the metamaterial. By continuously monitoring the output field of the probe mode, a photon is registered when the integrated homodyne signal exceeds a predetermined threshold. This approach shares similarities with the photodetector design introduced in Ref. [12], with the distinction that here the photon is probed *in flight* as

it travels through the metamaterial rather than after interaction with a localized absorber mode. This distinction is the key to achieving large detection fidelities without sacrificing bandwidth.

A noteworthy feature of this detector design is that although the detection bandwidth is large, the CRLH metamaterial can be engineered such as to have frequency cutoffs [30]. The low-frequency cutoff avoids the detector from being overwhelmed by low-frequency thermal photons. Moreover, hybridization of the meatamaterial waveguide and the probe resonator can happen due to imperfect quarton couplers. Although the quarton is nominally a purely nonlinear element, deviations from the ideal operation point due to flux variation, junction disorder, as well as stray capacitive couplings, all contribute to linear coupling between the metamaterial and probe resonator. The JTWPD can be designed to be robust to such stray linear couplings by placing the probe-mode resonance frequency to be outside of the metamaterial frequency band. In this situation, the metamaterial effectively acts as a Purcell filter for the probe mode, thereby avoiding degradation of the probe-mode quality factor.

III. BACKACTION AND DETECTOR NOISE

In the JTWPD, backaction on the incoming photon's wave vector, and therefore photon backscattering, is minimized by working with a giant probe, which minimizes information about the photon's position. Focusing first on the ideal case where the probe-mode self-Kerr nonlinearity K and the dispersive shift $\chi(x)$ can be neglected compared to $g(x) = \alpha\chi(x)$, we clarify the dominant noise process for the probe resonator and the associated backaction on the photon by deriving a perturbative master equation. In the subsequent section, we turn to full numerical analysis including the effect of the nonlinearities K and χ.

Considering the ideal case for the moment and ignoring the spatial dependence of $g(x)$, the interaction Hamiltonian takes the simple longitudinal-coupling form [33]

$$\hat{H}_{\text{ideal}} = \hbar g \sum_{\nu\mu} \int_{-z/2}^{z/2} dx \hat{b}_\nu^\dagger(x)\hat{b}_\mu(x)\left(\hat{a}^\dagger + \hat{a}\right). \quad (5)$$

We model the incoming photon by an emitter system with annihilation operator $\hat{c}$, $[\hat{c}, \hat{c}^\dagger] = 1$, located at $x_0 < -z/2$ and initialized in Fock state $|1\rangle$. The decay rate $\kappa_c(t)$ of the emitter to the transmission line is chosen such as to have a Gaussian wavepacket with center frequency $\bar{\omega}$ and FWHM γ propagating towards the detector [see Eq. (D1)]. Using Keldysh path integrals, we trace out the waveguide to find a perturbative master equation for the joint emitter-probe system. As discussed in Appendix D, to second order in the interaction, this master equation takes a remarkably simple form

$$\dot{\hat{\rho}} = -i\left[g n_{\text{det}}(t)(\hat{a} + \hat{a}^\dagger), \hat{\rho}_c\right] + \Gamma(t)\mathcal{D}[\hat{a} + \hat{a}^\dagger]\hat{\rho}_c + \kappa_c(t)\mathcal{D}[\hat{c}]\hat{\rho} + \kappa_a\mathcal{D}[\hat{a}]\hat{\rho}. \quad (6)$$

In this expression, $\mathcal{D}[\hat{o}]\bullet = \hat{o}\bullet\hat{o}^\dagger - 1/2\{\hat{o}^\dagger\hat{o}, \bullet\}$ is the usual Lindblad-form dissipator and we define $\hat{\rho}_c(t) = \hat{c}\hat{\rho}(t)\hat{c}^\dagger/\langle\hat{c}^\dagger\hat{c}\rangle(t)$,

$$n_{\text{det}}(t) = \frac{1}{v}\int_{-z/2}^{z/2} dx\, |\xi\,(x,t)|^2\,, \quad (7)$$

$$\Gamma(t) = \frac{4g^2}{\kappa_a v}\int_{-z/2}^{z/2} dx\left[1 - e^{-(\kappa_a/2v)[x+(z/2)]}\right]|\xi\,(x,t)|^2\,, \quad (8)$$

with $\xi(x,t) = \xi(t - x/v)$ the incoming photon envelop and $n_{\text{det}}(t)$ the fraction of the photon that is in the metamaterial at time t. A term of order $g/\bar{\omega}$ describing backscattering of the photon into the left-moving field is dropped from Eq. (6). With $\bar{\omega}$ the carrier frequency of the incoming photon, this contribution is negligible.

In Eq. (6), $\hat{\rho}_c$ is the state of the system *conditioned* on a photon having been emitted. The first term of Eq. (6) consequently has an intuitive interpretation: the probe resonator is conditionally displaced by a drive equal to the longitudinal coupling amplitude times the photon fraction in the metamaterial, $g \times n_{\text{det}}(t)$. Indeed, while the x quadrature of the probe, $\hat{x} = (\hat{a}^\dagger + \hat{a})/\sqrt{2}$, is a constant of motion under Eq. (6), the y quadrature, $\hat{y} = i(\hat{a}^\dagger - \hat{a})/\sqrt{2}$, is displaced.

The second term of Eq. (6), proportional to the rate $\Gamma(t)$, is the dominant process contributing to noise also along the y quadrature. The origin of the noise term can be understood as follows. When the photon first enters the detector and is only partially inside the metamaterial, the probe-mode field evolves to a superposition of being displaced to different average values of $\hat{y}$, leading to enhanced fluctuations in this quadrature. This effect can be seen clearly in the numerical results of Fig. 3, which are described in more detail below. Finally, the last line of Eq. (6) describes the usual decay of the emitter and probe at respective rates $\kappa_c(t)$ and κ_a.

As the increased fluctuations in the y quadrature arise due to uncertainty in the photon's position, a spatially longer photon is expected to lead to larger fluctuations. A measurement of the probe's y quadrature will collapse the superposition of displaced states and thus lead to a backaction effect localizing the photon and randomizing its wave vector. This effect can be minimized by decreasing the interaction strength g while keeping gz/v constant by increasing z. In other words, backaction can be minimized by increasing the detector length relative to the spatial extent of the photon. This intuitive reasoning is confirmed by numerical results in the next section.

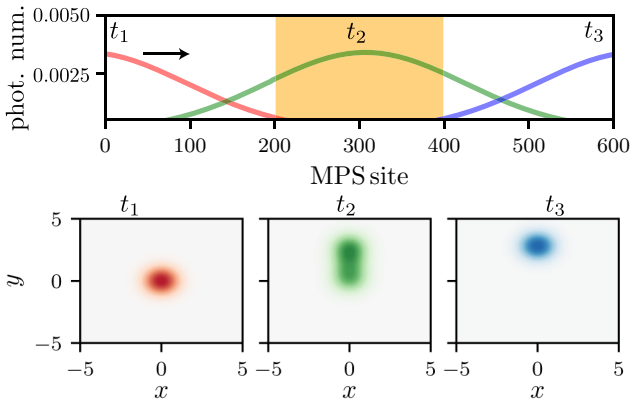

FIG. 3. The top panel shows snapshots of the photon-number population along the matrix-product-state (MPS) sites at three different times t_1 (red) $< t_2$ (green) $< t_3$ (blue). The white region corresponds to the linear waveguide and the orange region to the metamaterial with its coupling to the probe resonator. The bottom three panels show the Wigner function $W(x,y)$ of the intracavity probe field at the three respective times. When the photon is only partially inside the metamaterial, the probe is in a superposition of displaced states (middle panel). Parameters are $\kappa_a = \chi(x) = K = 0$, $g\tau = 2$, and $\gamma\tau = 2$.

IV. NUMERICAL MATRIX-PRODUCT-STATE SIMULATIONS

We now turn to numerical simulations of the JTWPD including the self- and cross-Kerr nonlinearities K and χ that we dropped in the preceding section. To go beyond the perturbative results of Eq. (6), it is no longer possible to integrate out the waveguide degrees of freedom. A brute-force numerical integration of the dynamics is, however, impractical, as the JTWPD is an open quantum many-body system with a large number of modes. We overcome this obstacle by using a numerical approach where the systems is represented as a stochastically evolving MPS conditioned on the homodyne measurement record of the probe output field.

Our approach is based on trotterizing the time evolution and discretizing the photon waveguide, including the nonlinear metamaterial, along the x axis. Building upon and extending recent developments of MPS in the context of waveguide QED [34,35], this leads to a picture where the waveguide is represented by a "conveyor belt" of harmonic oscillators (referred to as MPS sites below) interacting with the probe resonator. Measurement backaction under continuous homodyne detection of the probe resonator is included by representing the state as a quantum trajectory conditioned on the measurement record [36]. With our approach this is simulated using a stochastic MPS algorithm. Further details on this numerical technique can be found within the Supplemental Material [32].

As in the previous section, we consider a Gaussian photon wavepacket with FWHM γ propagating towards the detector by an emitter initialized in the state $|1\rangle$ localized to the left of the detector. The interaction strength is quantified by the dimensionless quantity $g\tau$, where $\tau = z/v$ is the interaction time as before, and the photon width by the dimensionless quantity $\gamma\tau$. Example snapshots of the photon-number distribution along the MPS sites at three different times $t_1 < t_2 < t_3$ are shown in Fig. 3, along with the corresponding Wigner functions of the probe-mode field. Because of the impedance match and negligible backaction, the photon population wavepacket travels without any deformation along the waveguide.

We start by comparing numerical results from MPS simulations to the perturbative master equation obtained in Eq. (6). To help in directly comparing the simulation results, we first consider the idealized situation, where $\chi(x) = K = 0, g(x) = g > 0$. In Fig. 4, we show the average probe resonator displacement $\langle\hat{y}\rangle$ whose integrated value is linked to the detector signal and the noise $\langle\Delta\hat{y}^2\rangle$ as a function of time. To verify the prediction that fluctuations in $\hat{y}$ increase for spatially longer photons, we compare Gaussian wavepackets of different spectral widths γ. Recall that a *smaller* $\gamma\tau$ implies a *longer* photon relative to the detector length. The solid lines in Fig. 4 are obtained using MPS simulations with $\gamma\tau = 2$ (blue), 4 (orange), 6 (green), and 10 (bright purple). The dotted lines are obtained from Eq. (6) for the same parameters. The agreement between the approximate analytical results and the full nonperturbative MPS results is remarkable.

A relevant question is how robust the detector is to spatial variations in the nonlinearity $g(x) = \alpha\chi(x)$. In a

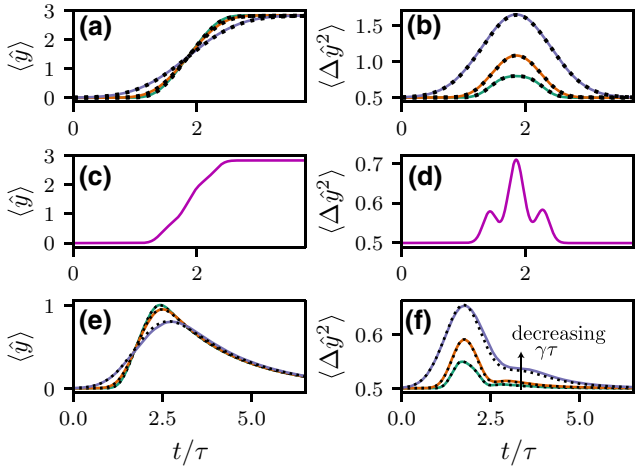

FIG. 4. Time evolution of the intracavity probe displacement $\langle\hat{y}\rangle$ [(a),(c),(e)] and fluctuations $\langle\Delta\hat{y}^2\rangle$ [(b),(d),(f)], in the idealized case $\chi(x) = K = 0$. Top row: $\kappa_a = 0$ and $g\tau = 2$. Middle row: $\kappa_a = 0$ and spatially varying $g(x)$ with average value $\bar{g}\tau = 2$. Bottom row: $\kappa_a\tau = 1.0$ and $g\tau = 2$. The solid lines correspond to MPS simulations with different photon widths $\gamma\tau = 2$ (blue), 4 (orange), 6 (green), and 10 (bright purple), while the dotted lines are from integrating Eq. (6).

physical realization, spatial variations can arise, e.g., due to disorder in the quarton-junction critical currents and variations in the flux through the quarton loops. Moreover, there is naturally a spatial dependence in $\chi(x)$ due to the spatial dependence of the probe resonator mode function (illustrated by blue arrows in Fig. 2). In (c),(d) of Fig. 4 we use a spatially varying $g(x)$, and we consequently show only MPS results in these panels. To confirm the robustness of the detector to this variation, Figs. 4(b) and 4(c) show $\langle\hat{y}\rangle$ and $\langle\Delta\hat{y}^2\rangle$ versus time as obtained from MPS simulations for $g(x) = 2\bar{g}\cos^2(2\pi x/z) + \mu(x)$. The cosine models the dependence on the mode function of a $\lambda/2$ resonator while $\mu(x)$ is added to take into account potential random variations in the coupling strength, which we take here to be as large as 10%. Moreover, to show the effect of a nonuniform $g(x)$ more clearly, we use $\gamma\tau = 10$ corresponding to spatially shorter photons than in the other panels. Although additional structures can now be seen, the long-time average displacement remains unchanged confirming that the detector is remarkably robust against spatial variations of the metamaterial-probe coupling.

Figures 4(e),(f) show results for $\kappa_a > 0$. In this situation the MPS evolves stochastically with each trajectory resulting in a measured current $J_{\rm hom}(t) = \sqrt{\kappa_a}\langle\hat{y}\rangle_{\rm traj} + \xi(t)$, where $\xi(t) = dW_t/dt$ with dW_t a Wiener process representing white noise [36]. We compare $\langle\hat{y}\rangle$ and $\langle\Delta\hat{y}^2\rangle$ averaged over one thousand stochastic trajectories to the results obtained by integrating the Keldysh master equation, Eq. (6). The agreement is excellent for large $\gamma\tau$, but small deviations are observed when this parameter is decreased. We attribute this to terms of higher than second order in the interaction Hamiltonian, which are neglected in Eq. (6). The exponential decay of $\langle\hat{y}\rangle$ at long time observed in (e) simply results from the finite damping rate κ_a. Indeed, the photon-induced displacement stops once the photon has traveled past the metamaterial at which point the probe mode relaxes back to its idle state.

For a given trajectory, we infer that a photon is detected if the homodyne current convolved with a filter [4],

$$\bar{J}_{\rm hom}(t) = \int_0^{\tau_m} dt' J_{\rm hom}(t') f(t'-t), \tag{9}$$

is larger than a threshold $y_{\rm thr}$, i.e., $\max_t \bar{J}_{\rm hom}(t) > y_{\rm thr}$. The filter $f(t) \propto \langle\hat{y}(t)\rangle$ is obtained from averaging over a large number of trajectories and is chosen such as to give more weight to times where the signal is on average larger. We maximize t over the time window $[-\tau_m, \tau_m]$ and choose the threshold to optimize between quantum efficiency and dark counts. The quantum efficiency η is defined as the probability of detecting a photon given that one was present. From the above procedure, it can be estimated as $\eta = N_{\rm click|1}/N_{\rm traj|1}$, with $N_{\rm click|1}$ the number of reported "clicks" and $N_{\rm traj|1}$ the number of simulated trajectories with a photon. On the other hand, the dark-count probability is estimated similarly as the fraction of reported clicks $p_D = N_{\rm click|0}/N_{\rm traj|0}$ in a simulation with no incoming photon. In these simulations, the dark-count rate is set by the threshold and the vacuum fluctuations of the probe resonator. A number that incorporates both η and p_D, and is thus a good measure of the performance of a photodetector, is the assignment fidelity [4]

$$\mathcal{F} = \frac{1}{2}(\eta + 1 - p_D). \tag{10}$$

In practice, if the arrival time of the photon is known to lie within some time window, one can optimize t in Eq. (9) over this window in a postprocessing step [12]. In our numerical simulations, the arrival time is known such that this optimization is not necessary and we can therefore simply evaluate $\bar{J}_{\rm hom}(t)$ at $t = 0$.

Figure 5 shows 75 typical filtered output records, $\bar{J}_{\rm hom}(t=0)$, as a function of the measurement window τ_m. These results are obtained from stochastic MPS simulations with $\gamma\tau = 6$, $g\tau = 3$, $\kappa_a\tau = 1.0$, and include self- and cross-Kerr couplings with $|K|/\kappa_a = 10^{-2}$ and $g/\chi = 5$. The red traces correspond to simulations where a photon was present, while the blue traces are for incoming vacuum. The horizontal gray line is the threshold chosen to optimize the assignment fidelity. At $\tau_m/\tau \gtrsim 3$, most traces are correctly identified. Panel (b) shows the assignment

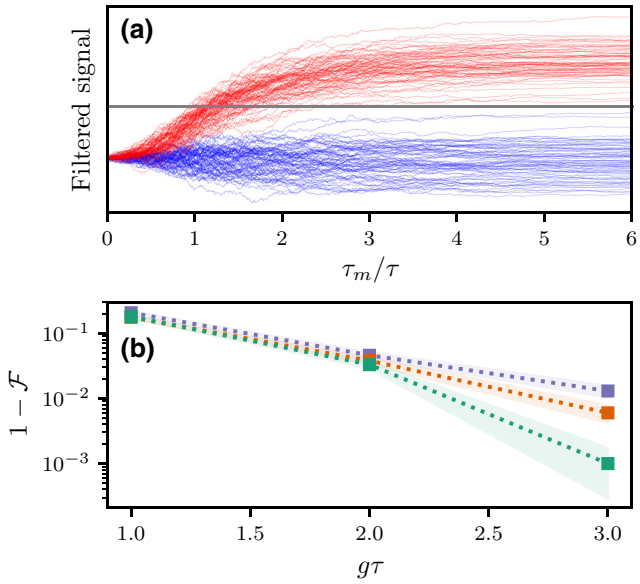

FIG. 5. (a) 75 filtered homodyne currents (arbitrary units) for $g\tau = 3$, $\kappa_a\tau = 1.0$, $|K|/\kappa_a = 10^{-2}$, and $g/\chi = 5$. Red traces are obtained with an incoming Gaussian photon of unitless width $\gamma\tau = 6$, and blue traces for vacuum. The horizontal gray line is the threshold chosen to maximize the assignment fidelity. (b) Infidelity versus $g\tau$ for $\gamma\tau = 2$ (blue), 4 (orange), and 6 (green), found by averaging over $N_{\rm traj} = 2000$ trajectories. Other parameters as in (a). The shaded regions indicate the standard error defined as $\pm\sqrt{\mathcal{F}(1-\mathcal{F})/N_{\rm traj}}$.

fidelity for $\gamma\tau = 2$ (blue), 4 (orange), and 6 (green) as a function of $g\tau$ but fixed $g/\chi = 5$. The measurement time τ_m is chosen sufficiently large to maximize $\mathcal{F}$. As expected from Fig. 4, the fidelity is reduced for smaller $\gamma\tau$ because spatially longer photons (smaller $\gamma\tau$) lead to more noise in the measurement.

A remarkable feature of Fig. 5 is the clear trend of the assignment fidelity approaching unity with increasing $g\tau$. This number can be increased at fixed τ by increasing g, or at fixed interaction strength g by increasing the detector length. (Note that the results in Fig. 5 are at fixed $\kappa_a\tau$, so that to match these simulations κ_a would have to be reduced for increasing τ. The reduction is, however, modest.) In the next section we show that values of $g\tau$ in the range 1–3 used in Fig. 5 are within reach for experimentally realistic parameters and metamaterial lengths.

V. TOWARDS EXPERIMENTAL REALIZATION

The JTWPD shares similarities with the Josephson traveling-wave parametric amplifier (JTWPA) [24,37,38]. State-of-the-art JTWPAs consist of a metamaterial with up to tens of thousands of unit cells, each comprised of a large Josephson junction and a shunt capacitance to ground. In addition, LC oscillators used to engineer the dispersion relation are placed every few unit cells. We envision a JTWPD with a similar number of unit cells, albeit with an increase in complexity for each unit cell. A significant design difference is that in the JTWPD every unit cell is coupled to the same probe resonator. In practice, this resonator can be a coplanar waveguide resonator or a three-dimensional (3D) cavity.

As shown within the Supplemental Material [32], the number of unit cells necessary to reach a given value of $g\tau$ can be approximated by

$$N_{\text{cells}} \simeq \frac{1}{2}\left(\frac{g\tau}{\alpha}\frac{R_K}{8\pi Z_0}\right)^2 \frac{\bar{\omega}^2}{K_Q E_Q/\hbar}, \tag{11}$$

where we neglect spatial dependence of the parameters for simplicity. In contrast to the simulation results presented above, we assume here that the detector is operated in reflection mode, effectively halving the number of unit cells needed for a given value of τ. In this expression, α is the displacement of the probe resonator as before, $R_K = h/e^2$ is the quantum of resistance, Z_0 the characteristic impedance of the metamaterial at the center frequency $\bar{\omega}$, and E_Q the nonlinear energy of the coupling elements (see Appendix A).

The parameter K_Q appearing in Eq. (11) is the self-Kerr nonlinearity of the resonator [see Eq. (A3)] due to the nonlinear couplers in Fig. 2. An interesting feature of the quarton-coupling element is that the self-Kerr is always positive $K_Q > 0$ [31], in contrast to a more conventional Josephson-junction element [39]. The total Kerr nonlinearity of the resonator can be adjusted by introducing another nonlinear element such as one or more Josephson junctions galvanically or capacitively coupled to the resonator. We can then write the total Kerr nonlinearity as $K = K_Q + K_J$, where $K_Q > 0$ is the contribution from the couplers in Fig. 2, and $K_J < 0$ comes from one or more Josephson junctions. The latter elements can be made tunable, allowing an *in situ* tuning of $K_J < 0$. Following this approach, we can allow for a detector with a larger K_Q contributing to reducing N_{cells}, yet still have a total Kerr nonlinearity $K \simeq 0$ to avoid nonlinear response of the probe mode. Similar ideas have recently been used to cancel unwanted cross-Kerr nonlinearities [40].

Figure 6 shows N_{cells} as a function of the self-Kerr K_Q to reach $g\tau$ in the range 1–3, for a photon center frequency of $\bar{\omega}/(2\pi) = 5$ GHz. In these plots we use a nonlinearity $I_s = E_Q/\varphi_0 = 1.1$ μA for the coupling element, cf. Appendix A, and the other parameters are $\alpha = 5$ and $Z_0 = 50$ Ω. For a quarton with $n_s = 3$ large junctions this corresponds to a critical current of $I_c = 3.7$ μA for each large junction and 1.2 μA for the smaller junction. Crucially, it is possible to reach $g\tau$ in the range 1–3, as in our numerical simulations above, using a few thousand unit cells without an excessively large K_Q. Alternatively, the same value of $g\tau$ can be reached for a smaller K_Q by increasing the transmission line characteristic impedance, Z_0, as is clear from Eq. (11). As discussed in more detail within the Supplemental Material [32], K_Q can be tuned by varying the coupling capacitance between the junctions and the probe resonator, or by tuning the characteristic impedance of the coupler mode.

The CRLH metamaterial has a frequency-independent characteristic impdeance $Z_0 = \sqrt{L_n/C_g}$ given that $\sqrt{L_n/C_g} = \sqrt{L_g/C_n}$, referred to as a balanced CRLH [30]. Close to the center of the CLRH frequency band, the dispersion relation is approximately linear, with a speed of light given by $v = 1/\sqrt{4L_nC_g}$. For typical parameters, discussed in more

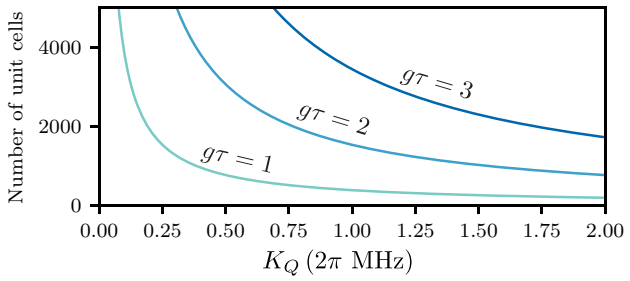

FIG. 6. Number of unit cells needed to reach $g\tau$ in the range 1–3 as a function of self-Kerr nonlinearity K_Q, for $\alpha = 5$, $\bar{\omega}/(2\pi) = 5$ GHz, $I_s = E_Q/\varphi_0 = 1.1$ μA, and $Z_0 = 50$ Ω. The total Kerr nonlinearity of the resonator $K = K_Q + K_J$ can be tuned close to zero by introducing another nonlinearity with $K_J < 0$.

detail in the Supplemental Material [32], we expect detection times in the range $\tau = 1$–10 μs. To have $\kappa_a \tau = 1$ as in the simulations above, this then suggests a probe decay rate in the range $\kappa_a/2\pi \simeq 0.015$–$0.15$ MHz. Larger values of $\kappa_a \tau$ might be preferable in practice, but we found this regime too demanding for numerical simulations due to the prohibitively small time steps needed. A larger κ_a relaxes the constraint on reducing the total self-Kerr nonlinearity $|K| = |K_Q + K_J|$, and might lead to faster detection and reset times.

Based on the numerical results in the previous section, the detection time is of the order $\tau_m \simeq 3\tau$, and thus expected to be in the μs to tens of μs range for the above mentioned value of τ. The detector reset time is naturally of the order $1/\kappa_a$, but can likely be made faster using active reset protocols. To avoid significant backaction effects, the photon's spectral width must not be too small as we show in the preceding sections. A value for the dimensionless photon width of $\gamma\tau = 2$ corresponds to a FWHM of $\gamma/(2\pi) = 0.25$ MHz, for the value $\tau = 1$ μs. We emphasize that the detection fidelity increases with increasing γ, and from our numerical results we thus expect photons of spectral width in the MHz range or larger to be detectable with very high fidelity.

The bandwidth of the detector is set by appropriately choosing the parameters of the CRLH metamaterial. In the Supplemental Material [32] we show example parameter sets with bandwidths ranging from several GHz to 100s of MHz. For some applications that require very low dark-count rates, lowering the bandwidth might be desirable. In principle, the CLRH bandwidth can be made arbitrarily small, but the circuit parameters required may become challenging to realize. Another option is to replace the coupling element shown in the inset of Fig. 2 by a floating coupler, such that the bandwidth is controlled by a coupling capacitance. All of these various options are discussed in more detail within the Supplemental Material [32].

A. Potential obstacles and limiting factors

We here briefly summarize the JTWPD design's robustness to various imperfections and key experimental challenges.

Imperfect quarton-coupling elements: the JTWPD is designed to be robust to imperfections in the nonlinear quarton-coupling elements. As discussed in Sec. IV, the JTWPD is highly robust to spatial variation in the nonlinear coupling $g(x)$, which can arise due to variation in critical current or flux in the quarton-coupling elements.

Realistically, the quarton couplers also lead to some stray capacitive and linear inductive coupling between the probe mode and the metamaterial. Degradation of the probe-mode quality factor can be minimized by placing the probe-mode frequency outside the metamaterial band. In the Supplemental Material [32], we study the effect of stray linear coupling in more detail for example parameter sets. The main conclusion of this study is that stray linear coupling leads to a small reduction in the cross-Kerr coupling $\chi(x)$, and opens a small band gap in the center of the JTWPD frequency band. The latter will reduce the effective bandwidth of the JTWPD, as the detector can not operate in, or close to, this band gap.

Metamaterial loss: the numerical results presented above neglects loss in the metamaterial. In practice, we expect that loss will limit the detection fidelity in a realistic device. Including loss in MPS simulations is challenging, and will be the subject of future work. In the Supplemental Material [32] we introduce loss in the Keldysh path-integral approach leading to a generalization of Eq. (6). The second-order Keldysh master equation retains the same form, but the integrands in Eqs. (7) and (8) are both reduced by a factor $\exp[-\alpha_{\rm det}(x + z/2)]$, where $\alpha_{\rm det}$ is the loss per unit length. Numerical solutions to the Keldysh master equation including loss shows that the displacement-to-fluctuation ratio $|\langle \hat{y}_{\rm photon}(t) - \hat{y}_{\rm no\ photon}(t)\rangle|/\sqrt{\langle \Delta\hat{y}^2_{\rm photon}(t)\rangle + \langle \Delta\hat{y}^2_{\rm no\ photon}(t)\rangle}$ suffers only a small reduction for a realistic value of loss. As a point of comparison, for the parameters used in Fig. 4, the reduction due to a realistic value of 1-dB distributed loss is much smaller than the corresponding reduction if the coupling strength is lowered from $g\tau = 2$ to $g\tau = 1$. These preliminary results suggest that realistic values of loss is not an obstacle to reaching detection fidelities well over 90%.

VI. DISCUSSION

Previous works have questioned whether cross-Kerr interaction can be used for high-fidelity, broadband single-photon counting [29], seemingly in contradiction with our results. There is, however, a fundamental difference between our proposal and the approach in Ref. [29]. There, a number of nonlinear absorbers *independently* couple to a traveling control field. This is similar to an alternative version of our proposal where each unit cell of the metematerial couples to an independent probe resonator. More generally, we can consider a situation where we partition the $N_{\rm cells}$ unit cells of the detector into M blocks, with each block coupled to an independent readout probe resonator. With $M = N_{\rm cells}$ we have a setup similar to Ref. [29], while $M = 1$ corresponds to the JTWPD. However, as shown in Appendix E, such a setup gives a $\sqrt{M}$ *reduction* in the probe resonator's displacement. Our proposal thus has an $\sqrt{N_{\rm cells}}$ improvement in the SNR scaling. This improvement comes from using what we refer to in the introduction as a giant probe, i.e., a probe resonator that has a significant length compared to the photon. This contrasts with conventional circuit QED-based photodectors relying on pointlike probe systems. Such a setup does not have any obvious analog in the optical domain, demonstrating the

potential of using metamaterials based on superconducting quantum circuits to explore new domains of quantum optics.

In summary, we introduce the JTWPD, a microwave single-photon detector based on a weakly nonlinear metamaterial coupled to a giant probe. This detector is unconditional in the sense that no *a priori* information about the photon arrival time or detailed knowledge of the photon shape is needed for its operation. Detection fidelities approaching unity are predicted for metamaterial length that are compatible with state-of-the-art experiments. Moreover, because the JTWPD does not rely on absorption into a resonant mode, large detection bandwidths are possible.

A remarkable feature of the JTWPD, which distinguishes this detector from photodetectors operating in the optical regime, is the nondestructive nature of the interaction. Our numerical simulations clearly show that the shape of the photon population wavepacket is minimally disturbed by the detection. Together with the large bandwidth and high detection fidelity, this opens possibilities for single-photon measurement and control, including feedback of photons after measurement, weak single-photon measurement, and cascading photon detection with other measurement schemes or coherent interactions.

ACKNOWLEDGMENTS

We thank J. Bourassa, T. Stace, J. Combes, and B. Plourde for valuable discussions. This work is supported by the Australian Research Council (ARC) via Centre of Excellence in Engineered Quantum Systems (EQUS) Project No. CE170100009 and a Discovery Early Career Researcher Award (DE190100380). Part of this work is supported by the Army Research Office under Grant No. W911NF-15-1-0421, NSERC, the Vanier Canada Graduate Scholarship, and by the Canada First Research Excellence Fund. This research is funded in part by the MIT Center for Quantum Engineering via support from the Laboratory for Physical Sciences under Contract No. H98230-19-C-0292.

APPENDIX A: NONLINEAR COUPLING ELEMENT

We make use of a circuit identical to a flux qubit, or equivalently the SNAIL element introduced in Ref. [41], but used at a different operating point where it has been dubbed a "quarton" [31]. The coupler consists of a loop of n_s large junctions with Josephson energy E_J and a single smaller junction with energy βE_J, leading to a nonlinear potential

$$\hat{U}_Q(\hat{\varphi}) = -\beta E_J \cos(\hat{\varphi} - \varphi_x) - n_s E_J \cos\left(\frac{\hat{\varphi}}{n_s}\right), \quad \text{(A1)}$$

where φ_x is the dimensionless flux encircled by the loop. The coupler is operated at the point $\varphi_x = \pi$ and $\beta = 1/n_s$ where the potential becomes

$$\hat{U}_Q(\hat{\varphi}) = \frac{E_Q}{24}\hat{\varphi}^4 + \ldots, \quad \text{(A2)}$$

and we introduce $E_Q = E_J(n_s^2 - 1)/n_s^3$. Here we expand the nonlinear potential around $\hat{\varphi} \simeq 0$, which is valid based on the fact that each end of the element is coupled to harmonic modes with small zero-point flux fluctuations. The crucial property of this coupler is that it provides a purely nonlinear quartic potential while the quadratic contribution cancels out. This minimizes hybridization between the metamaterial and the probe resonator in the JTWPD, and is an interesting operation point for nonlinear interaction in general [42]. In practice there will be deviations from the ideal operation point $\phi_x = \pi$, $\beta = 1/n_s$, but as we show within the Supplemental Material [32], the JTWPD is robust to such imperfections.

The grounded LC oscillator shown in the inset of Fig. 2 is used to control the frequency and impedance of the coupler mode, and thus the detuning from the probe resonator and the strength of the nonlinearity. By galvanically coupling the quarton to the metamaterial and capacitively to the probe resonator, we can optimize the trade-off between a large cross-Kerr coupling and a smaller self-Kerr for the probe mode. Example parameter sets and a detailed study of the dressed mode structure of the full probe-metamaterial system can be found in the Supplemental Material [32].

The positive quartic potential in Eq. (A2) leads to positive self- and cross-Kerr nonlinearities for the probe-metamaterial system, in contrast to more conventional Josephson-junction nonlinearities. In the Supplemental Material [32] we use a blackbox quantization approach [39] to estimate the Kerr nonlinearities. In particular, the self-Kerr nonlinearity of the probe mode induced by N_{cells} coupler elements takes the form

$$\hbar K_Q = \sum_{n=0}^{N_{\text{cells}}-1} E_{Q,n}|\varphi_r(x_n)|^4, \quad \text{(A3)}$$

with $E_{Q,n}$ the energy of the nth nonlinear coupler and $\varphi_r(x_n)$ the dimensionless zero-point flux fluctuations of the probe mode biasing the nth coupling element.

APPENDIX B: DYNAMICS OF THE PROBE RESONATOR

The probe-resonator Hamiltonian can be written as

$$\hat{H}_r = \hbar\omega_r \hat{a}^\dagger \hat{a} + \frac{\hbar K}{2}\hat{a}^{\dagger 2}\hat{a}^2 + \hbar\left(i\varepsilon e^{-i\omega_d t}\hat{a}^\dagger + \text{H.c.}\right), \quad \text{(B1)}$$

with $\hat{a}$ the annihilation operator for the probe mode satisfying $[\hat{a}, \hat{a}^\dagger] = 1$. The resonator frequency ω_r includes

significant frequency shifts due to the nonlinear couplers. Moreover, the Kerr nonlinearity $K = K_Q + K_J$ includes both a contribution $K_Q > 0$ coming from the N_{cells} coupler elements and a contribution $K_J < 0$, which can be used to cancel out $K \simeq 0$, as discussed in the main text. The last term of $\hat{H}_r$ describes a resonator drive with amplitude ε and frequency ω_d. Taking damping of the probe resonator into account, the dynamics of the system is described by the master equation

$$\dot{\rho} = -\frac{i}{\hbar}[\hat{H}, \rho] + \kappa_a \mathcal{D}[\hat{a}]\rho. \tag{B2}$$

Moving to a frame rotating at the drive frequency and then displacing the field such that $\hat{a} \to \hat{a} + \alpha$, $\hat{H}_r$ takes the form

$$\hat{H}_r'/\hbar = (\delta + 2K|\alpha|^2)\hat{a}^\dagger\hat{a} + \frac{K}{2}\hat{a}^{\dagger 2}\hat{a}^2, \tag{B3}$$

where $\delta = \omega_r - \omega_d$ and with α chosen such as to satisfy the steady-state equation

$$(\delta + K|\alpha|^2)\alpha - \frac{i\kappa_a}{2}\alpha + i\varepsilon = 0. \tag{B4}$$

To drive the probe mode on resonance despite the Kerr nonlinearity, we choose ω_d such that $\delta = -2K|\alpha|^2$. With this choice, the transformed probe Hamiltonian reduces to

$$\hat{H}_r' = \frac{\hbar K}{2}\hat{a}^{\dagger 2}\hat{a}^2, \tag{B5}$$

while the nonlinear equation for α becomes

$$K|\alpha|^2\alpha + \frac{i\kappa_a}{2}\alpha = i\varepsilon. \tag{B6}$$

For $K|\alpha|^2 \ll \kappa_a$, the solution is approximately $\alpha = 2\varepsilon/\kappa_a$ and the steady state of the resonator is to a good approximation the coherent state $|\alpha\rangle$. As discussed further within the Supplemental Material [32], in the opposite limit, the steady state becomes non-Gaussian something which can reduce the SNR of the detector. To remain in the linear regime for sizable α, we require $|K|/\kappa_a$ to be small. Note that the solution for α is in general complex, while we take α to be real in the main text, to simplify notation. This can, however, be done without loss of generality, since we can simply perform a canonical transformation $\hat{a} \to \hat{a}e^{-i\theta}$ with $\theta = \arg\alpha$ to eliminate the phase of α.

APPENDIX C: METAMATERIAL-PROBE CROSS-KERR COUPLING

In the laboratory frame, the cross-Kerr interaction between the probe resonator and the waveguide takes the form

$$\hat{H}_{\text{int}} = \hbar \sum_{\nu\mu} \int_{-z/2}^{z/2} dx\, \chi(x) \hat{b}_\nu^\dagger(x) \hat{b}_\mu(x) \hat{a}^\dagger \hat{a}, \tag{C1}$$

to fourth order in the Josephson nonlinear potentials Eq. (A2) and where $\nu = \pm$ refers to the direction of propagation of the photon. In this expression, we define the dispersive shift per unit length

$$\hbar\chi(x_n) = \frac{vE_{Q,n}}{a}\frac{4\pi Z_0}{R_K\bar{\omega}}|\varphi_r(x_n)|^2, \tag{C2}$$

with $\bar{\omega}$ the photon center frequency, Z_0 the characteristic impedance of the transmission line at frequency $\bar{\omega}$, and we recall that a is the unit cell length. Because we are only interested in small photon number in the waveguide, we safely drop fast-rotating terms and higher-order terms in $\hat{b}_{\nu\omega}$ from Eq. (C1). Moving to the rotating and displaced frame introduced for the probe resonator above, Eq. (C1) leads to Eq. (3), where $g(x) = \alpha\chi(x)$ with α given by Eq. (B6) and where we take α to be real to simplify notation.

The integral in $\hat{H}_{\text{int}}$ should be interpreted as a Riemann sum, and the continuum limit is valid as long as all relevant wavelengths are much longer than a. Moreover, the expression for $\hat{b}_\nu(x)$ in Eq. (4) and $\chi(x)$ in Eq. (C2) are derived under the assumption that dispersion is negligible over a relevant frequency band around $\bar{\omega}$, where the photon number is nonzero. In other words, we are working under the assumption that the incoming photon is sufficiently narrow. Nevertheless, we expect that photons with a large spread of frequency components compared to previous proposals can be detected.

APPENDIX D: EFFECTIVE KELDYSH MASTER EQUATION

We describe the main steps of the derivation leading to Eq. (6) and refer the reader to the Supplemental Material [32] for more details. We model the incoming photon using an emitter located at position x_0 to the left of the metamaterial with annihilation operator $\hat{c}$. After initializing the emitter in the state $|1\rangle$, the emitter decay rate, $\kappa_c(t)$, is chosen such as to model the desired single-photon wavepacket. Here, we choose a Gaussian wavepacket $\xi(t)$ of variance σ^2

$$\xi(t) = \left(\frac{2\sigma^2}{\pi}\right)^{1/4} e^{-i\bar{\omega}t} e^{-\sigma^2(t+x_0/v)^2}, \tag{D1}$$

by using [43]

$$\kappa_c(t) = \sqrt{\frac{8\sigma^2}{\pi}}\frac{e^{-2\sigma^2 t^2}}{1 - \text{erf}[\sqrt{2}\sigma t]}, \tag{D2}$$

with erf(x) the error function. The FWHM γ used in the main text is related to the variance as $\gamma = 2\sqrt{2\ln 2}\sigma$.

The ideal [setting $K = \chi = 0$ and ignoring spatial variation in $g(x)$] Hamiltonian for the detector, emitter, and waveguide is given by

$$\begin{aligned}\hat{H} &= \hat{H}_0 + \hat{H}_{\text{ideal}} + \hat{H}_c,\\ \hat{H}_0 &= \sum_{\nu}\int_{\Omega} d\omega\hbar\omega\hat{b}^{\dagger}_{\nu,\omega}\hat{b}_{\nu,\omega},\\ \hat{H}_{\text{ideal}} &= \hbar g\sum_{\nu\mu}\int_{-z/2}^{z/2} dx\hat{b}^{\dagger}_{\nu}(x)\hat{b}_{\mu}(x)(\hat{a}^{\dagger}+\hat{a}),\\ \hat{H}_c &= \bar{\omega}\hat{c}^{\dagger}\hat{c} + \sqrt{\kappa_c(t)v}\left[\hat{b}^{\dagger}_{+}(x_0)\hat{c} + \text{H.c.}\right].\end{aligned} \tag{D3}$$

Using this Hamiltonian and adding decay of the probe resonator, we write the corresponding Keldysh action following Ref. [44]. As explained in the Supplemental Material [32], to do this we take advantage of the fact that the action is quadratic in the fields $\hat{b}_{\pm}(x)$ and integrate out the waveguide degrees of freedom. The result is then expanded in a Taylor series in the interaction strength, which yields an effective Keldysh action for the emitter-resonator system. Finally, from that effective action, we find the equivalent master equation, Eq. (6).

APPENDIX E: DETECTOR RESPONSE NEGLECTING BACKACTION

To help build intuition for the detector's response to a single photon, it is useful to neglect backaction effects and any correlations between the emitter and detector. Under these approximations, upon tracing out the emitter from Eq. (6), we can replace the term $\text{tr}_C\left[\hat{c}\hat{\rho}\hat{c}^{\dagger}\right]$ by the approximate expression $\langle\hat{c}^{\dagger}\hat{c}\rangle\otimes\hat{\rho}_A$, where $\text{tr}_C\bullet$ is a partial trace over the emitter and $\hat{\rho}_A$ is the reduced state of the probe resonator. In this way, the reduced master equation for the probe resonator takes the form

$$\dot{\hat{\rho}}_A \simeq -i\left[gn_{\text{det}}(t)(\hat{a}+\hat{a}^{\dagger}),\hat{\rho}_A\right] + \kappa_a\mathcal{D}[\hat{a}]\hat{\rho}_A. \tag{E1}$$

The associated quantum Langevin equation is

$$\dot{\hat{a}} \simeq -ign_{\text{det}}(t) - \frac{\kappa_a}{2}\hat{a} + \sqrt{\kappa_a}\hat{a}_{\text{in}}(t), \tag{E2}$$

with $\hat{a}_{\text{in}}(t)$ the input field, which is in the vacuum state in the displaced frame, i.e., $\langle\hat{a}_{\text{in}}(t)\rangle = 0$. The solution for the expectation value $\langle\hat{a}(t)\rangle$ is then given by

$$\langle\hat{a}(t)\rangle \simeq -ig\int_{t_0}^{t} dt' e^{-\kappa_a(t-t')/2}n_{\text{det}}(t). \tag{E3}$$

As expected, the number of photon in the metamaterial, $n_{\text{det}}(t)$, leads to a displacement of the probe field. We have confirmed that for the parameters used in Fig. 4, the above approximate expression is indistinguishable from the solution found from the full Keldysh master equation [dotted lines in Figs. 4(a) and 4(e)].

1. Detectors in series

We can generalize the above discussion to a situation where the metamaterial is divided into M equal subsections, individually coupled to a set of M independent and identical probe resonators. The interaction Hamiltonian then takes the form

$$\hat{H}_{\text{ideal}} = \hbar g\sum_{m=0}^{M-1}\sum_{\nu\mu}\int_{x_m-\Delta x/2}^{x_{m+\Delta x/2}} dx\hat{b}^{\dagger}_{\nu}(x)\hat{b}_{\mu}(x)\left(\hat{a}^{\dagger}_m+\hat{a}_m\right), \tag{E4}$$

with $x_m = -z/2 + \left(m+\frac{1}{2}\right)\Delta x$, $\Delta x = z/M$, and $[\hat{a}_m, \hat{a}_n{}^{\dagger}] = \delta_{mn}$. Defining the collective mode

$$\hat{a}_{\Sigma} = \frac{1}{\sqrt{M}}\sum_{m=0}^{M-1}\hat{a}_m, \tag{E5}$$

satisfying $[\hat{a}_{\Sigma}, \hat{a}_{\Sigma}{}^{\dagger}] = 1$, and assuming that each probe resonator labeled by m couples identically with rate κ to a common input-output waveguide, leads to the quantum Langevin equation for the collective mode

$$\dot{\hat{a}}_{\Sigma} = \frac{i}{\hbar}[\hat{H}_{\text{ideal}},\hat{a}_{\Sigma}] - \frac{\kappa_{\Sigma}}{2}\hat{a}_{\Sigma} + \sqrt{\kappa_{\Sigma}}\hat{a}_{\text{in}}(t), \tag{E6}$$

where $\kappa_{\Sigma} = M\kappa$ and where we take the resonator frequencies to be identical. Under a similar set of approximations as above, we find

$$\dot{\hat{a}}_{\Sigma} \simeq -\frac{ig}{\sqrt{M}}n_{\text{det}}(t) - \frac{\kappa_{\Sigma}}{2}\hat{a}_{\Sigma} + \sqrt{\kappa_{\Sigma}}\hat{a}_{\text{in}}(t). \tag{E7}$$

Comparing to Eq. (E2), which is obtained for $M = 1$, we find a $\sqrt{M}$ reduction in the displacement. To compensate one could increase $g \to g\sqrt{M}$, but this leads to a breakdown of the assumption of negligible backaction. In summary the JTWPD limit $M = 1$ is ideal.

[1] F. Helmer, M. Mariantoni, E. Solano, and F. Marquardt, Quantum nondemolition photon detection in circuit qed and the quantum zeno effect, Phys. Rev. A **79**, 052115 (2009).

[2] Y.-F. Chen, D. Hover, S. Sendelbach, L. Maurer, S. Merkel, E. Pritchett, F. Wilhelm, and R. McDermott, Microwave Photon Counter Based On Josephson Junctions, Phys. Rev. Lett. **107**, 217401 (2011).

[3] S. R. Sathyamoorthy, L. Tornberg, A. F. Kockum, B. Q. Baragiola, J. Combes, C. Wilson, T. M. Stace, and G.

Johansson, Quantum Nondemolition Detection of a Propagating Microwave Photon, Phys. Rev. Lett. **112**, 093601 (2014).

[4] B. Fan, G. Johansson, J. Combes, G. Milburn, and T. M. Stace, Nonabsorbing high-efficiency counter for itinerant microwave photons, Phys. Rev. B **90**, 035132 (2014).

[5] K. Koshino, Z. Lin, K. Inomata, T. Yamamoto, and Y. Nakamura, Dressed-state engineering for continuous detection of itinerant microwave photons, Phys. Rev. A **93**, 023824 (2016).

[6] K. Inomata, Z. Lin, K. Koshino, W. D. Oliver, J.-S. Tsai, T. Yamamoto, and Y. Nakamura, Single microwave-photon detector using an artificial λ-type three-level system, Nat. Commun. **7**, 12303 (2016).

[7] A. Narla, S. Shankar, M. Hatridge, Z. Leghtas, K. Sliwa, E. Zalys-Geller, S. Mundhada, W. Pfaff, L. Frunzio, R. Schoelkopf, *et al.*, Robust Concurrent Remote Entanglement Between Two Superconducting Qubits, Phys. Rev. X **6**, 031036 (2016).

[8] O. Kyriienko and A. S. Sørensen, Continuous-Wave Single-Photon Transistor Based on a Superconducting Circuit, Phys. Rev. Lett. **117**, 140503 (2016).

[9] J. Leppäkangas, M. Marthaler, D. Hazra, S. Jebari, R. Albert, F. Blanchet, G. Johansson, and M. Hofheinz, Multiplying and detecting propagating microwave photons using inelastic cooper-pair tunneling, Phys. Rev. A **97**, 013855 (2018).

[10] S. Kono, K. Koshino, Y. Tabuchi, A. Noguchi, and Y. Nakamura, Quantum non-demolition detection of an itinerant microwave photon, Nat. Phys. **14**, 546 (2018).

[11] J.-C. Besse, S. Gasparinetti, M. C. Collodo, T. Walter, P. Kurpiers, M. Pechal, C. Eichler, and A. Wallraff, Single-Shot Quantum Nondemolition Detection of Individual Itinerant Microwave Photons, Phys. Rev. X **8**, 021003 (2018).

[12] B. Royer, A. L. Grimsmo, A. Choquette-Poitevin, and A. Blais, Itinerant Microwave Photon Detector, Phys. Rev. Lett. **120**, 203602 (2018).

[13] R. Lescanne, S. Deléglise, E. Albertinale, U. Réglade, T. Capelle, E. Ivanov, T. Jacqmin, Z. Leghtas, and E. Flurin, Irreversible Qubit-Photon Coupling for the Detection of Itinerant Microwave Photons, Phys. Rev. X **10**, 021038 (2020).

[14] A. Blais, A. L. Grimsmo, S. Girvin, and A. Wallraff, arXiv:2005.12667 (2020).

[15] A. A. Clerk, K. W. Lehnert, P. Bertet, J. R. Petta, and Y. Nakamura, Hybrid quantum systems with circuit quantum electrodynamics, Nat. Phys. **16**, 257 (2020).

[16] G. Burkard, M. J. Gullans, X. Mi, and J. R. Petta, Superconductor–semiconductor hybrid-circuit quantum electrodynamics, Nat. Rev. Phys. **2**, 129 (2020).

[17] Y. Kubo, F. R. Ong, P. Bertet, D. Vion, V. Jacques, D. Zheng, A. Dréau, J.-F. Roch, A. Auffeves, F. Jelezko, J. Wrachtrup, M. F. Barthe, P. Bergonzo, and D. Esteve, Strong Coupling of a Spin Ensemble to a Superconducting Resonator, Phys. Rev. Lett. **105**, 140502 (2010).

[18] M. Aspelmeyer, T. J. Kippenberg, and F. Marquardt, Cavity optomechanics, Rev. Mod. Phys. **86**, 1391 (2014).

[19] J. B. Spring, B. J. Metcalf, P. C. Humphreys, W. S. Kolthammer, X.-M. Jin, M. Barbieri, A. Datta, N. Thomas-Peter, N. K. Langford, D. Kundys, *et al.*, Boson sampling on a photonic chip, Science **339**, 798 (2013).

[20] N. H. Nickerson, J. F. Fitzsimons, and S. C. Benjamin, Freely Scalable Quantum Technologies Using Cells of 5-to-50 Qubits with Very Lossy and Noisy Photonic Links, Phys. Rev. X **4**, 041041 (2014).

[21] S. Lloyd, Enhanced sensitivity of photodetection via quantum illumination, Science **321**, 1463 (2008).

[22] S. K. Lamoreaux, K. A. van Bibber, K. W. Lehnert, and G. Carosi, Analysis of single-photon and linear amplifier detectors for microwave cavity dark matter axion searches, Phys. Rev. D **88**, 035020 (2013).

[23] R. H. Hadfield, Single-photon detectors for optical quantum information applications, Nat. Photonics **3**, 696 (2009).

[24] C. Macklin, K. O'Brien, D. Hover, M. Schwartz, V. Bolkhovsky, X. Zhang, W. Oliver, and I. Siddiqi, A near–quantum-limited josephson traveling-wave parametric amplifier, Science **350**, 307 (2015).

[25] L. Guo, A. Grimsmo, A. F. Kockum, M. Pletyukhov, and G. Johansson, Giant acoustic atom: A single quantum system with a deterministic time delay, Phys. Rev. A **95**, 053821 (2017).

[26] J. H. Shapiro, Single-photon kerr nonlinearities do not help quantum computation, Phys. Rev. A **73**, 062305 (2006).

[27] J. H. Shapiro and M. Razavi, Continuous-time cross-phase modulation and quantum computation, New J. Phys. **9**, 16 (2007).

[28] J. Gea-Banacloche, Impossibility of large phase shifts via the giant kerr effect with single-photon wave packets, Phys. Rev. A **81**, 043823 (2010).

[29] B. Fan, A. F. Kockum, J. Combes, G. Johansson, I.-c. Hoi, C. M. Wilson, P. Delsing, G. J. Milburn, and T. M. Stace, Breakdown of the Cross-Kerr Scheme for Photon Counting, Phys. Rev. Lett. **110**, 053601 (2013).

[30] C. Caloz, A. Sanada, and T. Itoh, A novel composite right-/left-handed coupled-line directional coupler with arbitrary coupling level and broad bandwidth, IEEE Trans. Microw. Theory Technol. **52**, 980 (2004).

[31] F. Yan, Y. Sung, P. Krantz, A. Kamal, D. K. Kim, J. L. Yoder, T. P. Orlando, S. Gustavsson, and W. D. Oliver, arXiv:2006.04130 (2020).

[32] See Supplemental Material at http://link.aps.org/supplemental/10.1103/PhysRevApplied.15.034074, which includes Refs. [45–55], for a detailed lumped-element treatment of the JTWPD and a derivation of the Keldysh master equation.

[33] N. Didier, J. Bourassa, and A. Blais, Fast Quantum Nondemolition Readout by Parametric Modulation of Longitudinal Qubit-Oscillator Interaction, Phys. Rev. Lett. **115**, 203601 (2015).

[34] A. L. Grimsmo, Time-Delayed Quantum Feedback Control, Phys. Rev. Lett. **115**, 060402 (2015).

[35] H. Pichler and P. Zoller, Photonic Circuits With Time Delays And Quantum Feedback, Phys. Rev. Lett. **116**, 093601 (2016).

[36] H. M. Wiseman and G. J. Milburn, *Quantum Measurement and Control* (Cambridge university press, Cambridge, England, 2009).

[37] T. White, J. Mutus, I.-C. Hoi, R. Barends, B. Campbell, Y. Chen, Z. Chen, B. Chiaro, A. Dunsworth, E. Jeffrey, *et al.*,

Traveling wave parametric amplifier with josephson junctions using minimal resonator phase matching, Appl. Phys. Lett. **106**, 242601 (2015).

[38] L. Planat, A. Ranadive, R. Dassonneville, J. Puertas Martínez, S. Léger, C. Naud, O. Buisson, W. Hasch-Guichard, D. M. Basko, and N. Roch, Photonic-Crystal Josephson Traveling-Wave Parametric Amplifier, Phys. Rev. X **10**, 021021 (2020).

[39] S. E. Nigg, H. Paik, B. Vlastakis, G. Kirchmair, S. Shankar, L. Frunzio, M. Devoret, R. Schoelkopf, and S. Girvin, Black-Box Superconducting Circuit Quantization, Phys. Rev. Lett. **108**, 240502 (2012).

[40] P. Mundada, G. Zhang, T. Hazard, and A. Houck, Suppression of Qubit Crosstalk in a Tunable Coupling Superconducting Circuit, Phys. Rev. Appl. **12**, 054023 (2019).

[41] N. Frattini, U. Vool, S. Shankar, A. Narla, K. Sliwa, and M. Devoret, 3-wave mixing josephson dipole element, Appl. Phys. Lett. **110**, 222603 (2017).

[42] Y. Ye, K. Peng, M. Naghiloo, G. Cunningham, and K. P. O'Brien, arXiv:2010.09959 (2020).

[43] J. E. Gough, M. R. James, H. I. Nurdin, and J. Combes, Quantum filtering for systems driven by fields in single-photon states or superposition of coherent states, Phys. Rev. A **86**, 043819 (2012).

[44] L. M. Sieberer, M. Buchhold, and S. Diehl, Keldysh field theory for driven open quantum systems, Rep. Prog. Phys. **79**, 096001 (2016).

[45] H. Wang, A. Zhuravel, S. Indrajeet, B. G. Taketani, M. Hutchings, Y. Hao, F. Rouxinol, F. Wilhelm, M. LaHaye, A. Ustinov, *et al.*, Mode Structure in Superconducting Metamaterial Transmission-Line Resonators, Phys. Rev. Appl. **11**, 054062 (2019).

[46] A. L. Grimsmo and A. Blais, Squeezing and quantum state engineering with josephson travelling wave amplifiers, npj Quantum Inf. **3**, 20 (2017).

[47] U. Vool and M. Devoret, Introduction to quantum electromagnetic circuits, Int. J. Circ. Theor. Appl. **45**, 897 (2017).

[48] N. A. R. Bhat and J. E. Sipe, Hamiltonian treatment of the electromagnetic field in dispersive and absorptive structured media, Phys. Rev. A **73**, 063808 (2006).

[49] V. Manucharyan, E. Boaknin, M. Metcalfe, R. Vijay, I. Siddiqi, and M. Devoret, Microwave bifurcation of a josephson junction: Embedding-circuit requirements, Phys. Rev. B **76**, 014524 (2007).

[50] J. Koch, M. Y. Terri, J. Gambetta, A. A. Houck, D. Schuster, J. Majer, A. Blais, M. H. Devoret, S. M. Girvin, and R. J. Schoelkopf, Charge-insensitive qubit design derived from the cooper pair box, Phys. Rev. A **76**, 042319 (2007).

[51] H. J. Carmichael, *Statistical Methods in Quantum Optics 1* (Springer-Verlag Berlin Heidelberg, Berlin, 2013).

[52] U. Schollwöck, The density-matrix renormalization group in the age of matrix product states, Ann. Phys. **326**, 96 (2011).

[53] C. Gardiner and P. Zoller, *Quantum Noise: A Handbook of Markovian and Non-Markovian Quantum Stochastic Methods with Applications to Quantum Optics* (Springer Series in Synergetics Springer, Berlin, 2000).

[54] H.-P. Breuer and F. Petruccione, *The Theory of Open Quantum Systems* (Oxford University Press on Demand, Oxford, England, 2002).

[55] P. E. Kloeden and E. Platen, *Numerical Solution of Stochastic Differential Equations* (Springer-Verlag Berlin Heidelberg, Berlin, 1992).